Supporting information

High valence state metal-ion doped Fe-Ni layered double hydroxide for oxygen evolution electrocatalyst and asymmetric supercapacitors

Wenke Shao, Qiufan Wang,* Can Huang, Daohong Zhang*

[a] *Key laboratory of Catalysis and Energy Materials Chemistry of Ministry of Education & Hubei Key Laboratory of Catalysis and Materials Science, Hubei R&D Center of Hyperbranched Polymers Synthesis and Applications, South-Central University for Nationalities, Wuhan 430074, China. Email: Zhangdh27@163.com* (D. Zhang)

Experimental section

Materials characterization. Electrode material properties were characterized by X-ray powder diffraction (XRD), X-ray photoelectron spectroscopy (XPS), scanning electron microscopy (SEM) and transmission electron microscopy (TEM). Cyclic voltammetry (CV), electrochemical impedance spectroscopy (EIS), and galvanostatic charge-discharge (GCD) measurements were carried out on an electrochemical workstation (Ivium, CompactState 10800).

Three-electrode electrochemical measurements. The positive or negative electrodes were fabricated by mixing with Fe-Ni_3Co_2 LDH or $FeSe_2$/C, super P and Polytetrafluoroethylene binder in a weight ratio of 7:2:1. Then the resultant slurries were coated onto the carbon cloth and dried at 60 °C for 12 h in a vacuum oven. In the three-electrode system, the as-prepared Fe-Ni_3M_x LDH or $FeSe_2$/C, a platinum electrode and a saturated calomel electrode (SCE) were used as the working electrode, counter electrode and reference electrode, respectively. A 3 M LiCl solution was used as an electrolyte for all electrochemical measurements. EIS was conducted on constant voltage mode by sweeping the frequency from 100 kHz to 0.01 Hz at an amplitude of 5 mV.

Preparation of all-solid-state ASC. The Fe-Ni_3Co_2 LDH and $FeSe_2$/C nanocomposite electrodes were coated with PVA/LiCl gel electrolyte three times and dried at 60 °C for 1 h, respectively. Two PVA/LiCl coated electrodes were placed in parallel together,

followed by coating with PVA/LiCl again to produce an all-solid-state ASC.

Electrochemical measurements

Electrocatalytic activities of prepared Fe-Ni_3M_x LDH electrode were measured in a three-electrode system with a CHI 760E electrochemical workstation at room temperature in 1.0 M KOH electrolyte for OER. 2 mg as-prepared catalysts and 2 mg Super P carbon black were dispersed in 800 μL deionized water, 180 μL isopropanol and 20 μL Nafion solution via ultrasonic treatment for 1 h to obtain a homogeneous dispersion. Subsequently, 7.85 μL of the resulting ink (containing 15.7 μg catalyst) was pipetted on the surface of glassy carbon (GC, 3mm) was used as a working electrode, a graphite rod was used as the counter electrode and Hg/HgO electrode was used as the reference electrode. Linear sweep voltammetry (LSV) curves were recorded at a scan rate of 5 mV s^{-1}. The cyclic voltammetry (CV) measurement was carried out with scan rates being increased from 10 to 100 mV s^{-1} in the potential range from 1 V to 1.1 V *vs.* RHE. Electrochemical impedance spectroscopy (EIS) data were recorded at an overpotential of 10 mA cm^{-2} from 0.01 Hz to 100 kHz under a 5 mV amplitude. For durability testing, 1000 cycles of CV test were performed between 1.326 and 1.626 V *vs.* RHE with a scan rate of 100 mV s^{-1}, and the LSV curves were recorded before and after the CV cycles were performed. Chronopotentiometric measurements were measured at a current density of 10 mA cm^{-2} for 10 h. In all measurements, the SCE reference electrode was calibrated with respect to reversible hydrogen electrode (RHE) using the equation: E(RHE) = E(SCE)+0.098+0.0591pH.

Density functional theory (DFT) calculation. All the spin theoretical simulations in our work were carried out on the Vienna ab initio Simulation Package (VASP) with the version 5.4.1. The Generalized gradient approximation (GGA) with the Perdew-Burke-Emzerhof (PBE) functional form was employed to evaluate the electron-electron exchange and correlation interactions while the projector augmented-wave (PAW) methods were implanted to represent the core-electron (valence electron) interactions. The GGA+U calculation were performed with the on-site Coulomb repulsion U term on the Ni 3d, Co 3d, Fe 3d, the Ueff (Ueff=U-J) values are 6.2 eV, 3.32 eV, 5.3 eV, respectively. Plane-Wave basis function was set with a kinetic cut-off energy of 550

eV. The ground-state atomic geometries were optimized by relaxing the force below 0.02 eV/Å and the convergence criteria for energy was set with the value of 1.0×10^{-5} eV/cell. A Monkhorst-Pack meshes with the size of $3 \times 3 \times 1$ were employed to sample surface Brillouin zone. Gaussian method was employed for the both electronic structures and total energy of our models and stress/force relaxations. In order to better describe the interactions between molecules, van der Waal (vdw) interactions are included descripting by DFT-D3 method of Grimme.

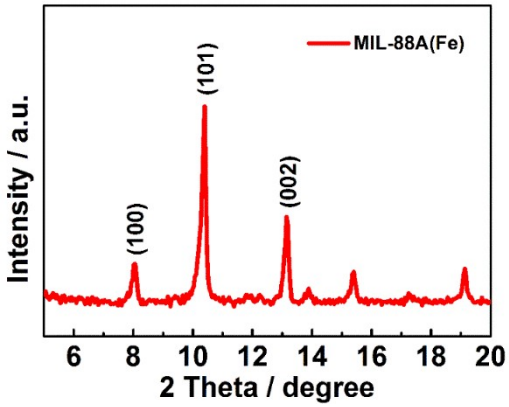

Fig. S1 XRD patterns of MIL-88A.

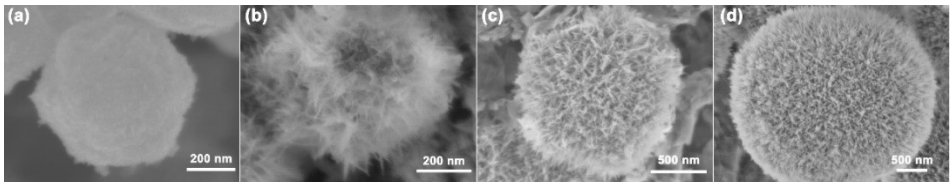

Fig. S2 SEM images of Fe-Ni_3Co_2 LDH with different reaction time (a) 0.5 h, (b) 2 h, and (c) 4 h, (d) 6 h.

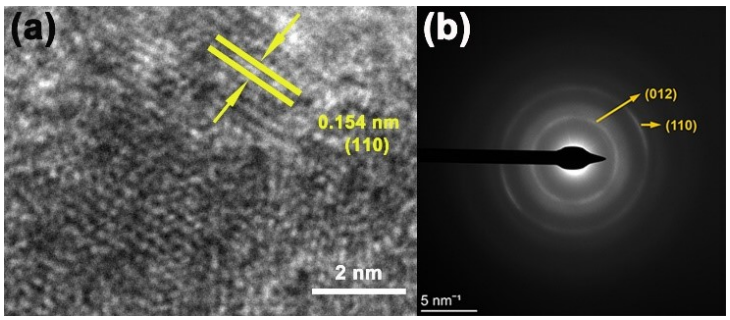

Fig. S3 (a) The high-TEM image and (b) the SAED pattern of Fe-Ni_3Co_2 LDH.

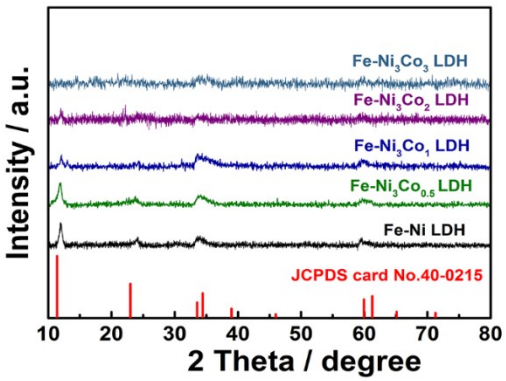

Fig. S4 XRD patterns of Fe-Ni_3Co_x LDH. (x=0, 0.5, 1, 2 and 3).

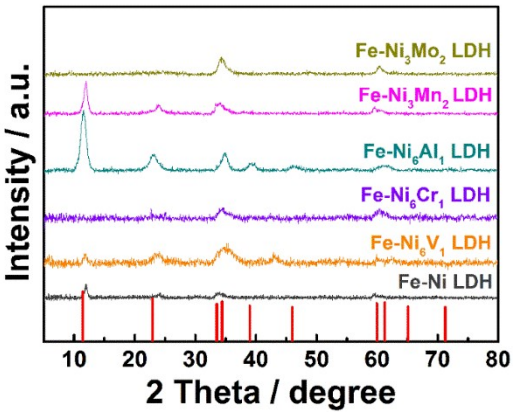

Fig. S5 XRD patterns of Fe-Ni_3M_x LDH. (M=V, Cr, Al, Mn, Mo).

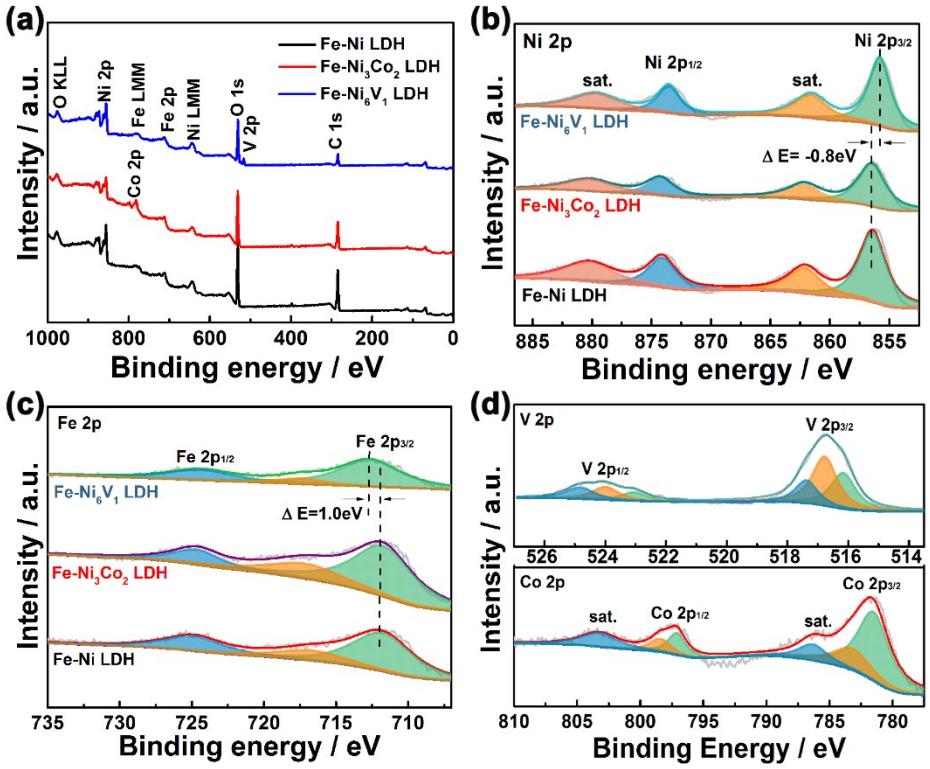

Fig. S6 XPS of (a) survey spectrum, (b) Ni 2p, (c) Fe 2p in Fe-Ni LDH, Fe-Ni_3Co_2

LDH and Fe-Ni_6V_1 LDH, and of (d) Co 2p in Fe-Ni_3Co_2 LDH, V 2p in Fe-Ni_6V_1 LDH.

The signals of elemental Ni, Fe, Co/V, and O were detected in the overall XPS spectra of Fe-Ni_3Co_2 LDH (red line in Fig. S6a) and Fe-Ni_6V_1 LDH (blue line in Fig. S6a), which match well with the elemental mapping results. In addition to two shakeup satellites, the Ni 2p spectra of pristine Fe-Ni LDH shown in Fig. S6b is composed of a pair of peaks with binding energies at 856.4 and 874.1 eV, corresponding to the Ni^{2+} $2p_{3/2}$ and Ni^{2+} $2p_{1/2}$, respectively[1]. Compared with that of Fe-Ni LDH, the main peak for Ni^{2+} $2p_{3/2}$ in Fe-Ni_3Co_2 LDH has no shift, but it shows a negative shift of about 0.8 eV in Fe-Ni_6V_1 LDH. The Fe $2p_{3/2}$ peak for Fe-Ni_6V_1 LDH in Fig. S6c corresponds to Fe^{3+}, which shows a positive shift to 712.7 eV from 711.7 eV for that in Fe-Ni LDH, indicating the chemical environment of iron ion and nickel ion was modified by doping vanadium into the laminate[2-3]. In Fig. S6d, with two shakeup satellites, the XPS spectrum of Co 2p is divided into two spin-orbit doublets of Co^{3+} and Co^{2+}. The main peaks located at 798.0 eV for Co $2p_{1/2}$ and 782.0 eV for Co $2p_{3/2}$ could be split into two distinct peaks of Co^{2+} (assigning to the 796.9 eV peak in Co $2p_{1/2}$ and the 781.5 eV peak in Co $2p_{3/2}$) and Co^{3+} (corresponding to the 798.3 eV peak in Co $2p_{1/2}$ and the 783.2 eV peak in Co $2p_{3/2}$)[4]. The high-resolution V 2p spectrum was also decomposed into V $2p_{3/2}$ and V $2p_{1/2}$ due to the spin-orbit splitting that separated by ~7.2 eV. Three components could be distinguished at 516.1 eV (in green), 516.8 eV (in orange) and 517.4 eV (in blue) were in good agreement with respectively V^{3+}, V^{4+} and V^{5+}, respectively[5]. These observations suggest the partial electron transfer from Ni and Fe to V in the Fe-Ni_6V_1 LDH through oxygen bridges (O^{2-}) between metal ions[6]. The XPS spectroscopy of the negative electrode was employed to evaluate further information on the structure of $FeSe_2$/C in Fig. S7.

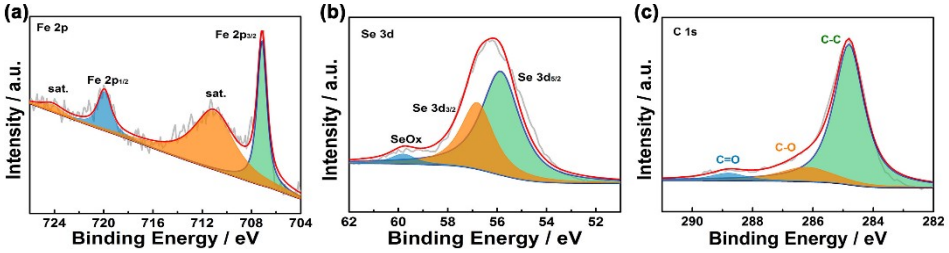

Fig. S7 (a-c) Fe 2p, Se 3d, C 1s XPS spectra of $FeSe_2$/C.

In Fig. S7a, a couple of peaks at 707.1 and 719.9 eV were associated with Fe $2p_{3/2}$ and Fe $2p_{1/2}$. And others at 711.1 and 724.2 eV were ascribed to satellite (Sat.) peaks[7]. The peak binding energy at 55.8 eV (Se $3d_{5/2}$) and 56.8 (Se $3d_{3/2}$) eV, respectively. The Se-O bond was observed at 59.8 eV confirming that a small amount of SeO_2 impurities was formed[8] (Fig. S7b). Fig. S7c showed the C 1s spectrum, three fitting peaks located at 284.8, 286.2, and 288.8 eV were attributed to C-C, C-O and C=O bond from amorphous carbon.

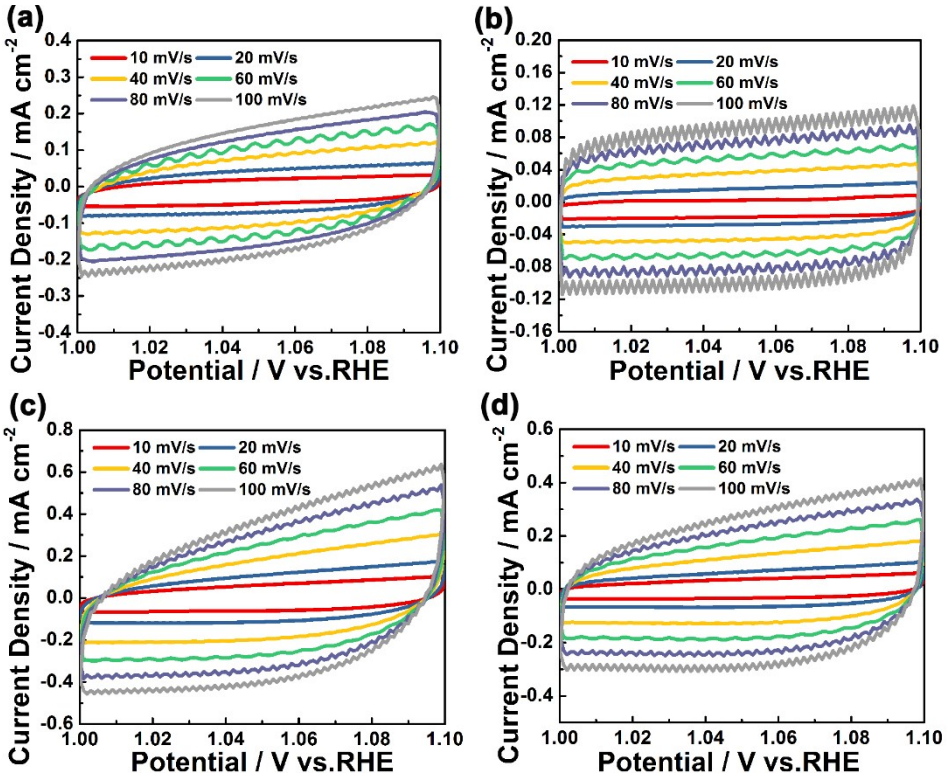

Fig. S8 Cyclic voltammograms (1-1.1 V vs. RHE) of Fe-Ni_3Cox, x =0 (a), x =1 (b), x =2 (c), and x =3 (d) LDH recorded in 1 M KOH.

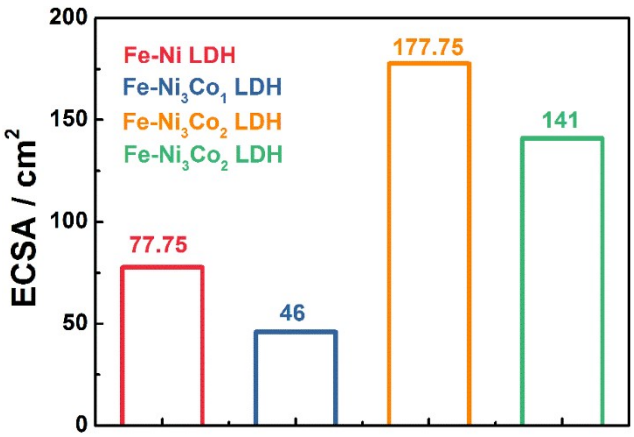

Fig. S9 the corresponding bar graph of the ECSA-normalized current density.

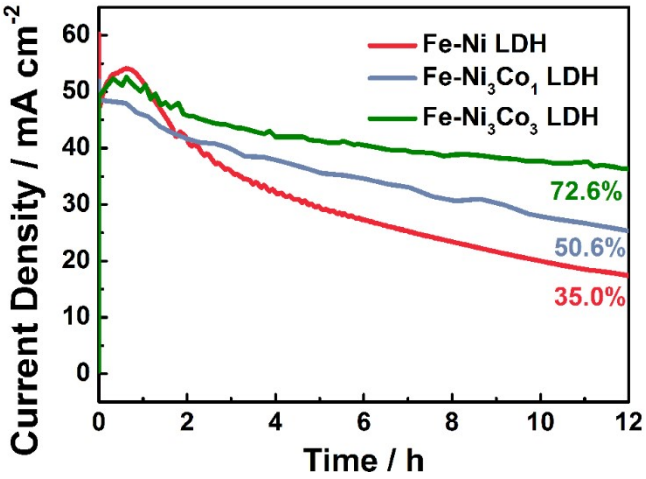

Fig. S10 The chronoamperometry curves of Fe-Ni LDH, Fe-Ni_3Co_1 LDH and Fe-Ni_3Co_3 LDH at the overpotential (50 mA cm^{-2}).

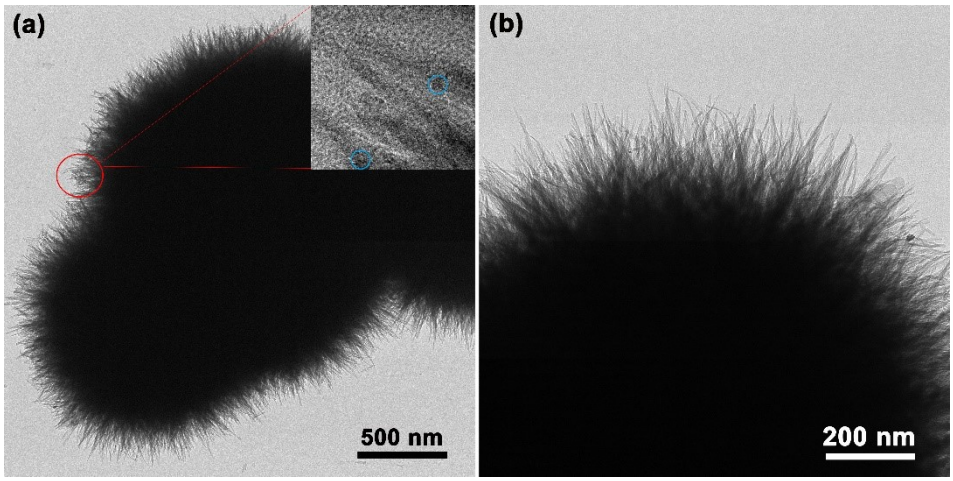

Fig. S11 (a) TEM images of Fe-Ni_3Co_2 LDH after 12 h durability test.

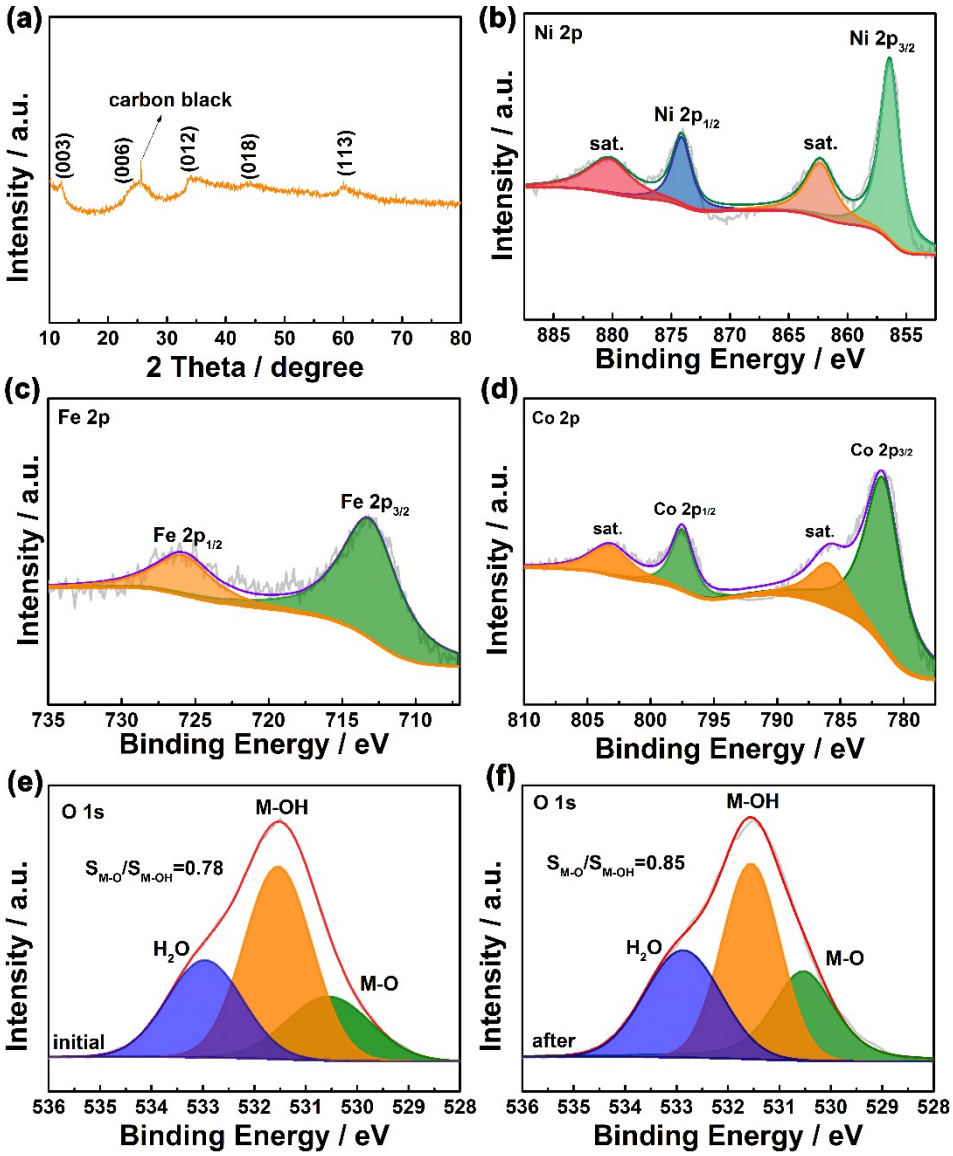

Fig. S12 (a) XRD pattern, XPS of (b) Ni 2p, (c) Fe 2p, (d) Co 2p of Fe-Ni_3Co_2 LDH after 12 h durability test. (e and f) O1s of Fe-Ni_3Co_2 LDH before and after 12 h durability test.

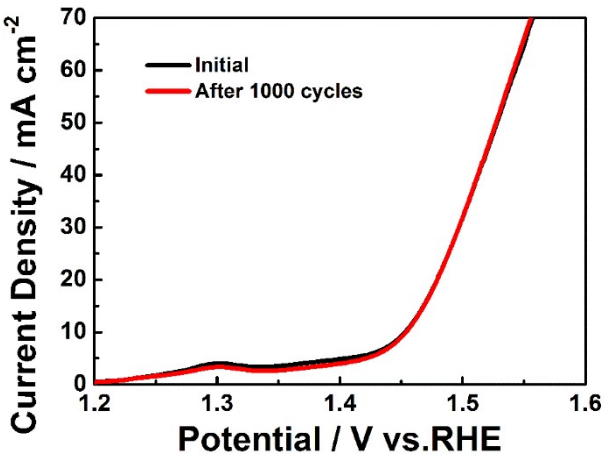

Fig. S13 LSV curves of Fe-Ni_3Co_2 LDH before (black) and after (red) 1000 CV cycles.

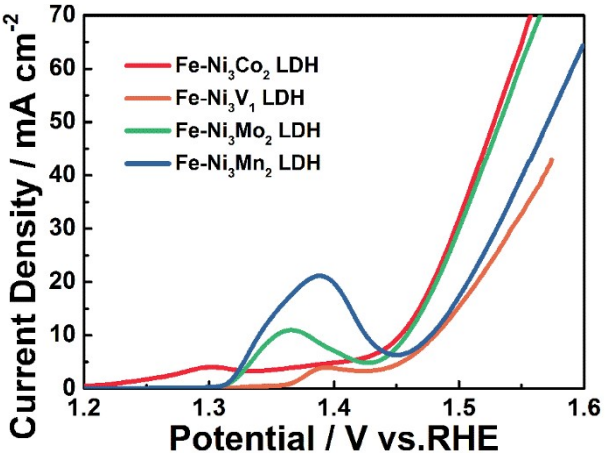

Fig. S14 LSV curves of Fe-Ni_3Co_2 LDH and Fe-Ni_3M LDH (M = V, Mo, and Mn) LDH synthesized using the same method in 1.0 M KOH electrolyte.

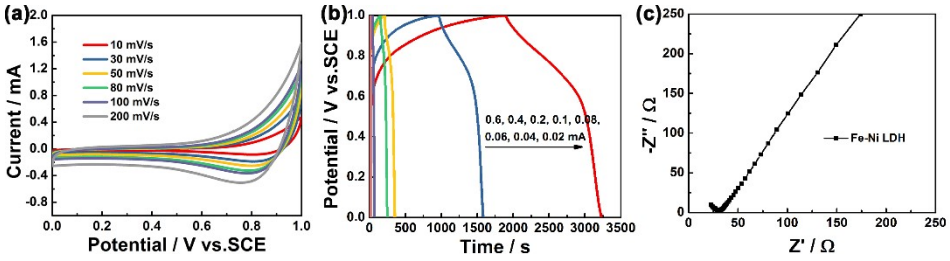

Fig. S15 (a) The cyclic voltammetry (CV) curves, (b) the galvanostatic Charge-discharge (GCD) curves, (c) Nyquist plots of Fe-Ni LDH.

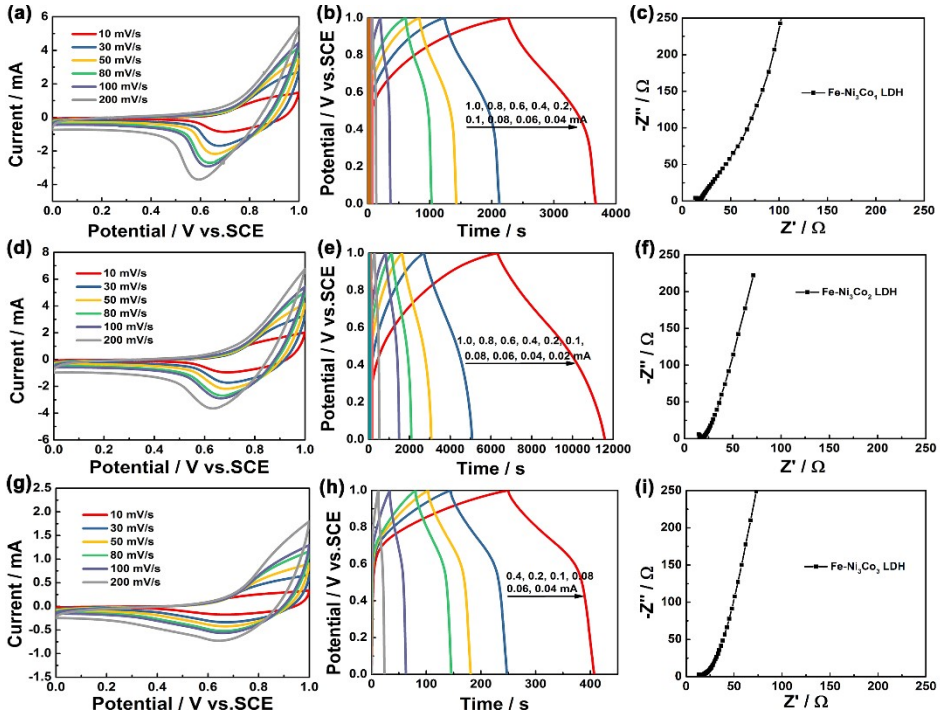

Fig. S16 The cyclic voltammetry (CV) curves, the galvanostatic Charge-discharge (GCD) curves and Nyquist plots of (a-c) Fe-Ni_3Co_1 LDH, (d-f) Fe-Ni_3Co_2 LDH, (g-i) Fe-Ni_3Co_3 LDH.

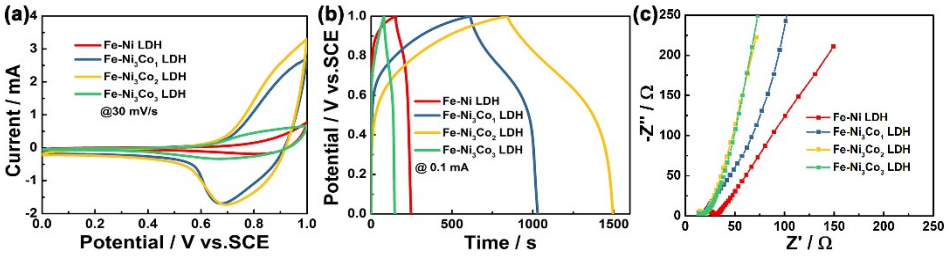

Fig. S17 (a) The CV curves of Fe-Ni_3Co_x (x=0,1,2 and 3) LDH at 10 mV s^{-1}, (b) The GCD curves of Fe-Ni_3Co_x (x=0,1,2 and 3) LDH at 0.1 mA, (c) Nyquist plots of Fe-Ni_3Co_x (x=0,1,2 and 3) LDH.

The CV diagrams of Fe-Ni_3Co_x LDH electrodes with different reactants ratios were shown in Fig. S17a within the voltage window of 0~1 V (*vs.* Hg/HgO) at 30 mV s^{-1}. It can be observed that the Fe-Ni_3Co_2 LDH electrode material has the largest area. Combined with the GCD curves (Fig. S17b) of these electrode materials when the current density is 0.1 mA, it can be concluded that the specific capacitance of Fe-Ni_3Co_2 LDH electrode material is the largest. It can prove that the tri-metal cation doping materials have better electrochemical performance than pristine bimetallic LDH, which is not only because the high valence state dopants create more active sites, but also the structure of bimetallic LDH has been tuned, producing strong synergistic effects between the doping cations and the host cations. This result is consistent with the above characterization analysis. Fig. S17c shows the Nyquist plots of the Fe-Ni_3Co_x LDH electrodes. Compared with other electrodes, Fe-Ni_3Co_2 LDH resistance is the smallest, which may due to its uniform nano-noodles structure facilitating surface electron transport and improving the electrical conductivity of the material.

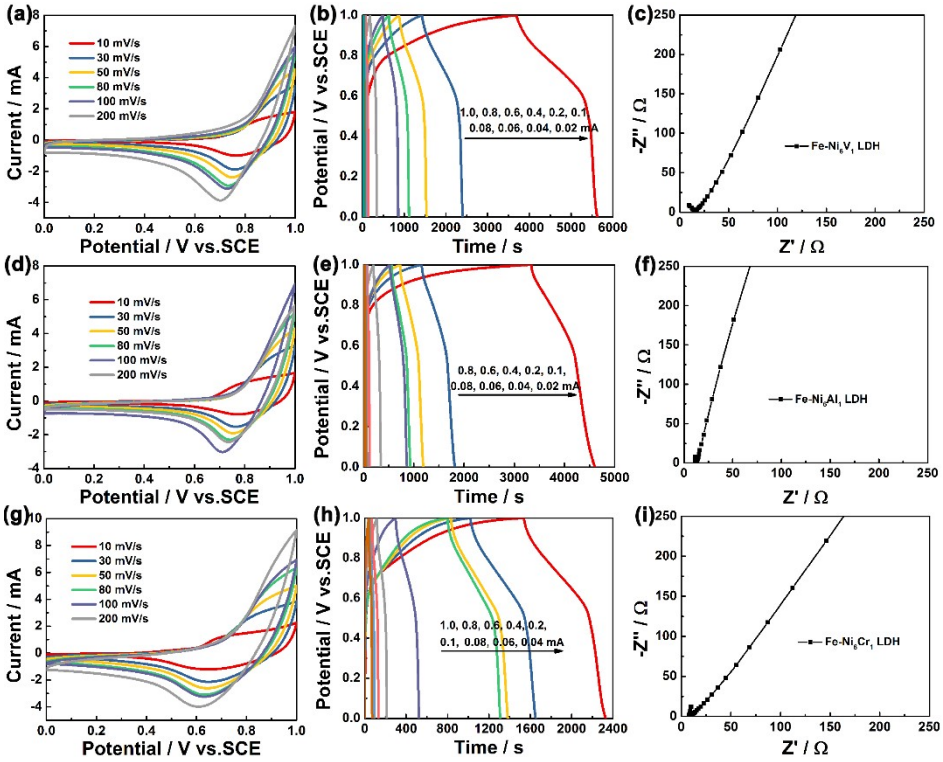

Fig. S18 The electrochemical performance of Fe-Ni_6M_1 LDH. (a) M=V, (b) M=Al, (c) M=Cr.

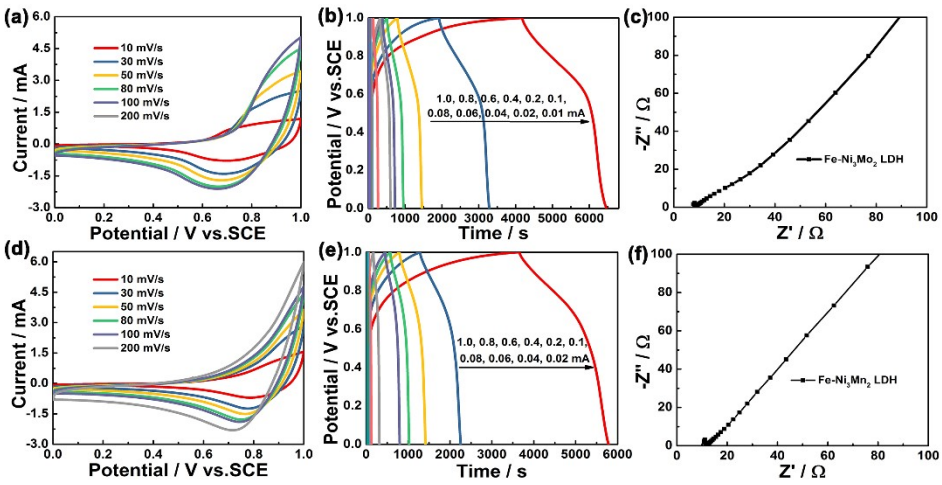

Fig. S19 The electrochemical performance of Fe-Ni_3M_2 LDH. (a) M=Mo, (b) M=Mn.

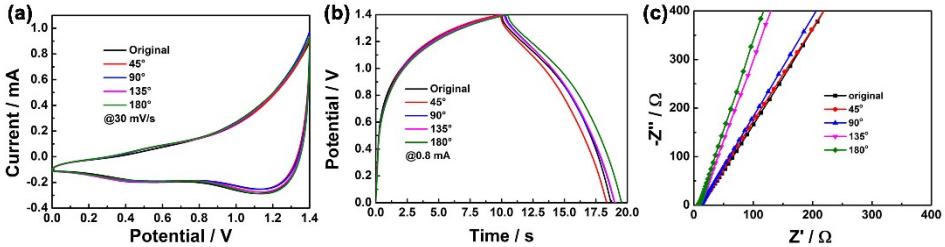

Fig. S20 CV curves at 30 mV/s, (b) GCD curves at 0.8 mA, and (c) Nyquist plots of ACS device under different bending angles from 0° to 180°, respectively.

Table S1. Comparison of the percentage of Fe, Co and Ni in the materials

	Fe / %	Ni / %	Co / %	V / %
Fe-Ni LDH	2.06	9.68	/	/
Fe-Ni_3Co_2 LDH	3.81	7.92	3.17	/
Fe- Ni_6V_1 LDH	2.28	17.23	/	2.71

Table S2. Comparison of OER activity of trimetallic Fe-Ni_3Cox LDH with state-of-the-art and some transition metal-based electrocatalysts reported in the literature.

Electrocatalysts	Electrolyte	Overpotential at 10 mA cm^{-2} (mV)	Tafel slope (mV dec^{-1})	Ref.
Fe-Ni_3Co_2 LDH	1 M KOH	224	73	This work
Fe-Ni LDH	1 M KOH	227	78	This work
Fe-Ni_3Co_1 LDH	1 M KOH	230	80	This work
Fe-Ni_3Co_3 LDH	1 M KOH	237	82	This work
RuO_2	1 M KOH	369	/	[9]
IrO_2	1 M KOH	338	/	[9]
IrO_x	1M NaOH	320	/	[10]
Commercial 20% Ir/C	0.1 M KOH	360	/	[11]
Porus monolayer NiFe-LDH	1M KOH	230	47	[12]
monolayer NiFe-LDH	1M KOH	272	54	
ZnCo-UF	1M KOH	360	66	[13]
Co_3O_4/2D Ti_3C_2 MXene heterojunctions	1M KOH	300	118	[14]

Reference

1. Wang, D.; Li, Q.; Han, C.; Lu, Q.; Xing, Z.; Yang, X., Atomic and electronic modulation of self-supported nickel-vanadium layered double hydroxide to accelerate water splitting kinetics. *Nat Commun* **2019,** *10* (1), 3899.

2. Li, P.; Duan, X.; Kuang, Y.; Li, Y.; Zhang, G.; Liu, W.; Sun, X., Tuning electronic structure of nife layered double hydroxides with vanadium doping toward high efficient electrocatalytic water oxidation. *Advanced Energy Materials* **2018,** *8* (15), 1703341.

3. Liu, Y.; Bai, Y.; Han, Y.; Yu, Z.; Zhang, S.; Wang, G.; Wei, J.; Wu, Q.; Sun, K., Self-supported hierarchical FeCoNi-LTH/$NiCo_2O_4$/CC electrodes with enhanced bifunctional performance for efficient overall water splitting. *ACS Appl Mater Interfaces* **2017,** *9* (42), 36917-36926.

4. Han, J.; Zhang, J.; Wang, T.; Xiong, Q.; Wang, W.; Cao, L.; Dong, B., Zn doped FeCo layered double hydroxide nanoneedle arrays with partial amorphous phase for efficient oxygen evolution reaction. *ACS Sustainable Chemistry & Engineering* **2019,** *7* (15), 13105-13114.

5. Luo, H.; Wang, B.; Wang, F.; Yang, J.; Wu, F.; Ning, Y.; Zhou, Y.; Wang, D.; Liu, H.; Dou, S., Anodic oxidation strategy toward structure-optimized V_2O_3 cathode via electrolyte regulation for Zn-ion storage. *ACS Nano* **2020,** *14* (6), 7328-7337.

6. Jiang, J.; Sun, F.; Zhou, S.; Hu, W.; Zhang, H.; Dong, J.; Jiang, Z.; Zhao, J.; Li, J.; Yan, W.; Wang, M., Atomic-level insight into super-efficient electrocatalytic oxygen evolution on iron and vanadium co-doped nickel (oxy)hydroxide. *Nat Commun* **2018,** *9* (1), 2885.

7. Ji, C.; Liu, F.; Xu, L.; Yang, S., Urchin-like $NiCo_2O_4$ hollow microspheres and $FeSe_2$ micro-snowflakes for flexible solid-state asymmetric supercapacitors. *Journal of Materials Chemistry A* **2017**, *5* (11), 5568-5576.

8. Ye, W.; Wang, K.; Yin, W.; Chai, W.; Tang, B.; Rui, Y., Rodlike $FeSe_2$–C derived from metal organic gel wrapped with reduced graphene as an anode material with excellent performance for lithium-ion batteries. *Electrochimica Acta* **2019**, *323*.

9. Zhang, R.; Sun, Z.; Zong, C.; Lin, Z.; Huang, H.; Yang, K.; Chen, J.; Liu, S.; Huang, M.; Yang, Y.; Zhang, W.; Chen, Q., Increase of Co 3d projected electronic

density of states in $AgCoO_2$ enabled an efficient electrocatalyst toward oxygen evolution reaction. *Nano Energy* **2019**, *57*, 753-760.

10. McCrory, C. C.; Jung, S.; Peters, J. C.; Jaramillo, T. F., Benchmarking heterogeneous electrocatalysts for the oxygen evolution reaction. *J Am Chem Soc* **2013**, *135* (45), 16977-87.

11. Mosa, I. M.; Biswas, S.; El-Sawy, A. M.; Botu, V.; Guild, C.; Song, W.; Ramprasad, R.; Rusling, J. F.; Suib, S. L., Tunable mesoporous manganese oxide for high performance oxygen reduction and evolution reactions. *Journal of Materials Chemistry A* **2016**, *4* (2), 620-631.

12. Zhang, X.; Zhao, Y.; Zhao, Y.; Shi, R.; Waterhouse, G. I. N.; Zhang, T., A Simple Synthetic Strategy toward Defect-Rich Porous Monolayer NiFe-Layered Double Hydroxide Nanosheets for Efficient Electrocatalytic Water Oxidation. *Advanced Energy Materials* **2019**, *9* (24).

13. Jia, X.; Zhang, X.; Zhao, J.; Zhao, Y.; Zhao, Y.; Waterhouse, G. I. N.; Shi, R.; Wu, L.-Z.; Tung, C.-H.; Zhang, T., Ultrafine monolayer Co-containing layered double hydroxide nanosheets for water oxidation. *Journal of Energy Chemistry* **2019**, *34*, 57-63.

14. Lu, Y.; Fan, D.; Chen, Z.; Xiao, W.; Cao, C.; Yang, X., Anchoring Co_3O_4 nanoparticles on MXene for efficient electrocatalytic oxygen evolution. *Science Bulletin* **2020**, *65* (6), 460-466.